The Astrophysical Journal Letters, 912:L11 (11pp), 2021 May 1 https://doi.org/10.3847/2041-8213/abf7cb

Thiols in the Interstellar Medium: First Detection of HC(O)SH and Confirmation of C_2H_5SH

Lucas F. Rodríguez-Almeida[1], Izaskun Jiménez-Serra[1], Víctor M. Rivilla[1,2], Jesús Martín-Pintado[1], Shaoshan Zeng[3], Belén Tercero[4], Pablo de Vicente[4], Laura Colzi[1,2], Fernando Rico-Villas[1], Sergio Martín[5,6], and Miguel A. Requena-Torres[7,8]
[1] Centro de Astrobiología (CSIC-INTA), Ctra Ajalvir km 4, E-28850 Torrejón de Ardoz, Madrid, Spain; lrodriguez@cab.inta-csic.es
[2] INAF-Osservatorio Astrofisico di Arcetri, Largo Enrico Fermi 5, I-50125 Florence, Italy
[3] Star and Planet Formation Laboratory, Cluster for Pioneering Research, RIKEN, 2-1 Hirosawa, Wako, Saitama 351-0198, Japan
[4] Observatorio de Yebes (IGN), Cerro de la Palera s/n, E-19141 Guadalajara, Spain
[5] Eureopean Southern Observatory, Alonso de Córdova 3107, Vitacura 763 0355, Santiago, Chile
[6] Joint ALMA Observatory, Alonso de Córdova 3107, Vitacura 763 0355, Santiago, Chile
[7] University of Maryland, College Park, MD 20742-2421, USA
[8] Department of Physics, Astronomy and Geosciences, Towson University, Towson, MD 21252, USA
Received 2021 February 10; revised 2021 April 14; accepted 2021 April 14; published 2021 April 30

Abstract

The chemical compounds carrying the thiol group (-SH) have been considered essential in recent prebiotic studies regarding the polymerization of amino acids. We have searched for this kind of compound toward the Galactic Center quiescent cloud G+0.693–0.027. We report the first detection in the interstellar space of the trans-isomer of monothioformic acid (t-HC(O)SH) with an abundance of $\sim 1 \times 10^{-10}$. Additionally, we provide a solid confirmation of the gauche isomer of ethyl mercaptan (g-C_2H_5SH) with an abundance of $\sim 3 \times 10^{-10}$, and we also detect methyl mercaptan (CH_3SH) with an abundance of $\sim 5 \times 10^{-9}$. Abundance ratios were calculated for the three SH-bearing species and their OH analogs, revealing similar trends between alcohols and thiols with increasing complexity. Possible chemical routes for the interstellar synthesis of t-HC(O)SH, CH_3SH, and C_2H_5SH are discussed, as well as the relevance of these compounds in the synthesis of prebiotic proteins in the primitive Earth.

Unified Astronomy Thesaurus concepts: Astrochemistry (75); Chemical abundances (224); Interstellar molecules (849); Galactic center (565)

1. Introduction

Among different theories of origin of life, one recurrent conundrum is the abiotic polymerization of amino acids since it requires ribosomes, macromolecular machines containing ribonucleic acid (RNA) and proteins. How could the first proteins form if they were needed to synthesize others? Following the ideas of Foden et al. (2020), a possible solution involves a thiol-based scenario in which SH-bearing molecules, together with the family of thioacids (R-C(O)SH) and thioesters (R-S-R′), have important properties as energy carriers and catalysts (Chandru et al. 2016; Leman & Ghadiri 2017). Although these types of compounds could be created in situ by an H_2S-mediated chemistry under prebiotically plausible conditions on early Earth (Shalayel et al. 2020), they also could have been delivered exogenously. Hence, observations of thiol-based molecules in space could shed some light on the availability of such compounds on a primitive Earth, and on their role in the prebiotic synthesis of proteins.

More than 220 molecules have been detected in the interstellar medium (ISM) and circumstellar shells[9] to date. However, sulfur-containing species only account for 20 of them. Furthermore, while molecules detected carrying C, H, or N range from 2 up to 13 atoms, the vast majority of S-bearing molecules have, at most, 4 atoms (such as H_2CS; Sinclair et al. 1973). This could be due to the relatively low cosmic abundance of atomic sulfur ($\approx 10^{-5}$ with respect to H_2, that is, more than 10 times lower than C or O; Asplund et al. 2009) together with its ability to have many different oxidation states and allotropes when compared to the more abundant elements (Jiménez-Escobar et al. 2014; Shingledecker et al. 2020) and its capacity of depleting fast in dense molecular clouds (Laas & Caselli 2019).

As a consequence, very few S-bearing molecules containing more than four atoms have firmly been detected in the ISM so far. One example is methyl mercaptan (hereafter CH_3SH), which has been detected in several environments, such as prestellar cores (Gibb et al. 2000), massive star-forming regions like Sagittarius B2 (Linke et al. 1979; Müller et al. 2016), and Solar-like protostars (Majumdar et al. 2016). The other one is ethyl mercaptan (hereafter C_2H_5SH), which was tentatively detected toward Orion KL (Kolesniková et al. 2014). Other searches for complex S-bearing molecules were unsuccessful, such as CH_3CHS (thioacetaldehyde; Margulès et al. 2020), NH_2CHS (thioformamide; Motiyenko et al. 2020), and $CH_3SC(O)H$ (S-methyl thioformate; Jabri et al. 2020).

In this Letter, we report the first detection in the ISM of the trans-isomer of monothioformic acid (hereafter HC(O)SH), the simplest thiol acid. We also report a solid confirmation of the gauche isomer of C_2H_5SH, together with the detection of CH_3SH. These molecules are found toward the quiescent Giant Molecular Cloud G+0.693–0.027 located in the Galactic Center (hereafter G+0.693). This source shows a very rich chemistry with up to 40 different complex organic molecules[10] detected (see, e.g., Requena-Torres et al. 2008; Rivilla et al. 2018, 2019; Zeng et al. 2018; Rivilla et al. 2020; Jiménez-Serra et al. 2020). Studies suggest that this cloud could be undergoing a cloud–

[9] https://cdms.astro.uni-koeln.de/classic/molecules

[10] These are usually referred as carbon-based molecules that have six or more atoms (Herbst & Van Dishoeck 2009).

cloud collision (Zeng et al. 2020), which induces large-scale shocks that sputter dust grains and that enhances the gas-phase abundance of molecules by several orders of magnitude (Requena-Torres et al. 2006).

2. Observations

We have used a spectral line survey toward G+0.693 covering several windows between 32 GHz to 172 GHz with an average resolution of 1.5 km s^{-1}, although the final spectral resolution employed in the figures has been smoothed up to 3 km s^{-1}. We stress that this is for a proper line visualization and does not alter in any form the analysis done.

For the observations, we used both the IRAM 30 m telescope located at Pico Veleta (Granada, Spain) and the Yebes 40 m telescope[11] (Guadalajara, Spain). The equatorial coordinates of the molecular cloud G+0.693 are α(J2000.0) = 17^{h}47^{m}22^{s} and δ(J2000.0) = −28°21′27″. The position switching mode was used in all the observations with the off position located at (−885″, 290″) from the source. The line intensity of the spectra was measured in units of T_A^* as the molecular emission toward G+0.693 is extended over the beam (Requena-Torres et al. 2006; Martín et al. 2008; Rivilla et al. 2018). In all the observations, each frequency setup was repeated shifting the central frequency by 20–100 MHz in order to identify spurious lines or contamination from the image band.

The IRAM 30 m observations were performed during three different sessions in 2019: April 10–16, August 13–19, and December 11–15. The dual polarization receiver EMIR was used connected to the fast Fourier transform spectrometers (FFTSs), which provided a channel width of 200 kHz in the 3 and 2 mm radio windows. The observations with the Yebes 40 m radiotelescope were carried out in 2020: from February 3 to 9 and from February 15 to 22. In this case, the Nanocosmos *Q*-band (7 mm) HEMT receiver was used, which enables ultra-broadband observations in two linear polarizations (Tercero et al. 2021). The receiver was connected to 16 FFTSs providing a channel width of 38 kHz and an instantaneous bandwidth of 18.5 GHz per polarization, covering the frequency range between 31.3 GHz and 50.6 GHz.

3. Analysis and Results

We used the software MADCUBA[12] (Martín et al. 2019) to perform the data analysis and line identification The Spectral Line Identification and Modelling (SLIM) tool of MADCUBA uses the spectroscopic data entries from different molecular catalogs, and generates a synthetic spectra based under the assumption of local thermodynamic equilibrium (LTE) conditions, and considering line opacity effects. The fitted parameters used to reproduce the molecular emission are column density (N), excitation temperature (T_{ex}), local standard of rest velocity (v_{LSR}), and FWHM.

Both HC(O)SH and C_2H_5SH have two rotamers, associated with the rotation of their respective C-S bond. HC(O)SH has one cis (c-HC(O)SH) and one trans (t-HC(O)SH) rotamer, the former being ∼330 K higher in energy (Hocking & Winnewisser 1976). C_2H_5SH has two degenerated ± gauche isomers (g-C_2H_5SH) and one antiperiplanar.

For our analysis we have used the following spectroscopic entries from the the CDMS[13] catalog: entries 062515/062516 for trans/cis isomers of HC(O)SH (Hocking & Winnewisser 1976), 062523/062524 for gauche/anti isomers of C_2H_5SH (Kolesniková et al. 2014; Müller et al. 2016), and 048510 for CH_3SH (Xu et al. 2012; Zakharenko et al. 2019).

3.1. Detection of t-HC(O)SH

The fitting procedure was performed considering the total emission of any other identified molecule in the spectral survey. This evaluation was carried out introducing all the compounds already detected in the ISM and in G+0.693 (see Requena-Torres et al. 2006, 2008; Zeng et al. 2018; Rivilla et al. 2019; Jiménez-Serra et al. 2020). For the analysis, it was also assumed a cosmic microwave background temperature (T_{bg}) of 2.73 K and no background continuum source (Zeng et al. 2020).

The global fit of all rotational lines to the observed data is shown in blue lines in Figure 1, while in red we show the fit of the individual lines of t-HC(O)SH, and the observational data in black. As shown in both Figure 1 and Table 1, we have detected a total of nine a-type transitions in the 7 mm and 3 mm bands, each one of them detected above the 5σ level in integrated intensity. Note that the SLIM synthetic spectrum shows small deviations with respect to the observations. These deviations are larger that the ones obtained for CH_3SH and g-C_2H_5SH (see Figures 3 and 4 in Appendix A). This is due to the fact that the t-HC(O)SH lines are significantly weaker than those of CH_3SH and g-C_2H_5SH (3–7 mK versus 5–12 mK and >40 mK, respectively). However, the fit of all clean t-HC(O)SH lines is consistent with the noise. We also note that for the three slightly blended lines of t-HC(O)SH, the contribution of the other molecules is less than 10% of the total intensity. Despite that the remaining two appear blended, the predicted LTE intensities are consistent with the observed lines. Note that the rest of the t-HC(O)SH lines covered within the observed frequency range are not shown due to strong blending issues.

The physical parameters obtained from the fit are listed in Table 2. The values obtained for T_{ex} and FWHM are consistent with those obtained previously for other molecular species toward this cloud (T_{ex} ∼ 5–20 K and line widths around 20 km s^{-1}; Zeng et al. 2018; Rivilla et al. 2020). The low T_{ex} indicates that the emission of the molecules in G+0.693 is subthermally excited as a result of the low H_2 densities of this source (T_{kin} ∼ 150 K; Requena-Torres et al. 2006; Zeng et al. 2018).

For t-HC(O)SH, the fitted column density gives (1.6 ± 0.1)× 10^{13} cm^{-2}. In addition, we derived a 3σ upper limit of ⩽3 × 10^{12} cm^{-2} for c-HC(O)SH (Table 2), as no clear transition has been detected within our data set. For the calculation, we have assumed the same T_{ex}, v_{LSR}, and FWHM as for t-HC(O)SH. A ratio c-HC(O)SH/t-HC(O)SH ⩽ 0.2 was obtained.

3.2. Detection of g-C_2H_5SH and CH_3SH

This molecule was tentatively detected in Orion KL (Kolesniková et al. 2014), based on a few isolated transitions assigned to this isomer. We report here an unambiguous detection of this isomer that confirms it presence in the ISM. We have listed in Table 4 (Appendix A) the transitions measured toward G+0.693. Note that eight of the targeted lines

[11] Yebes Observatory is operated by the Spanish Geographic Institute (IGN, Ministerio de Transportes, Movilidad y Agencia Urbana).

[12] MAdrid Data CUBe Analysis is a software developed at the Center of Astrobiology in Madrid: https://cab.inta-csic.es/madcuba/Portada.html.

[13] Cologne Database for Molecular Spectroscopy (Endres et al. 2016), https://cdms.astro.uni-koeln.de/classic/.

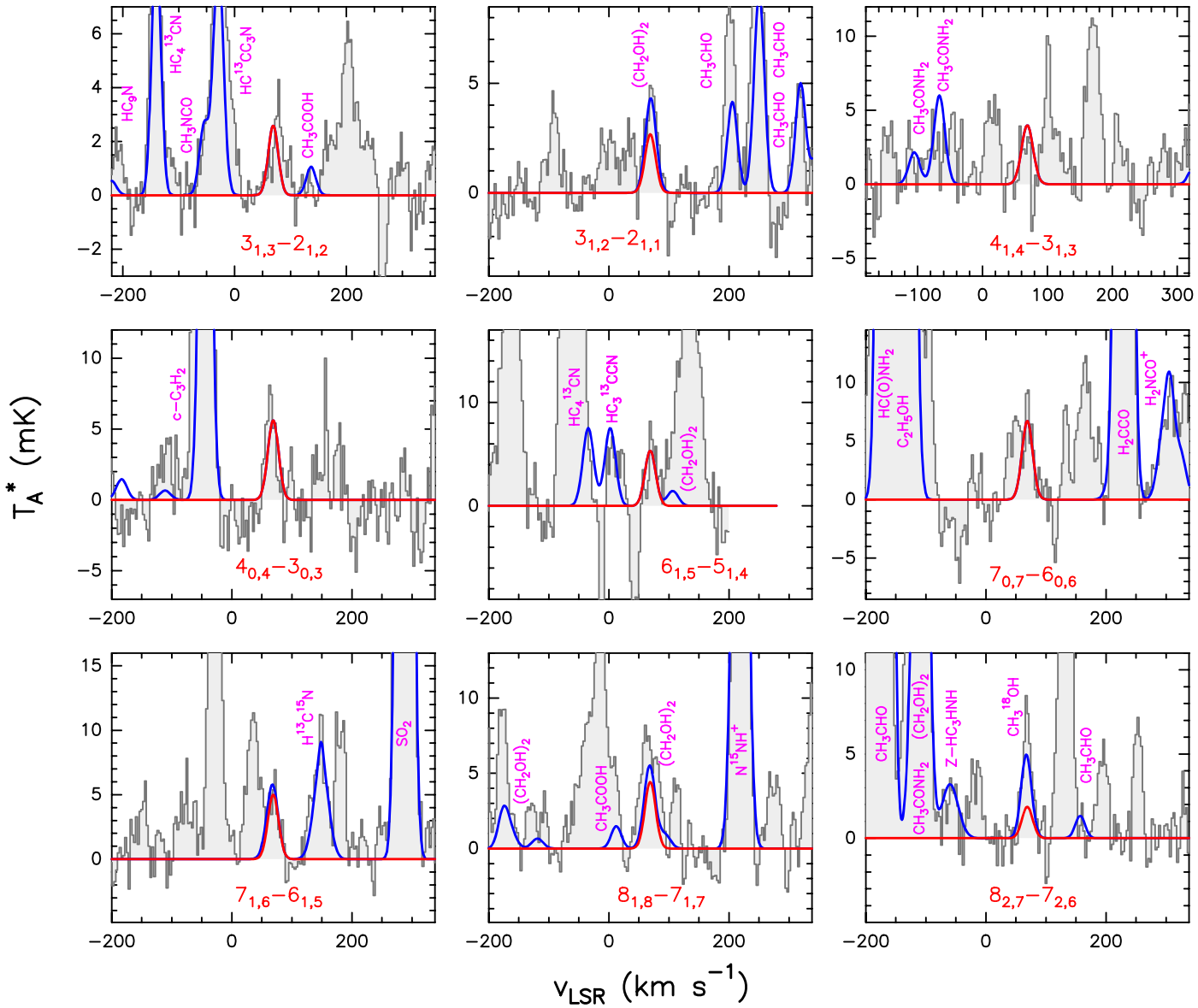

Figure 1. Cleanest and brightest lines of t-HC(O)SH detected toward G+0.693 labeled with their corresponding quantum numbers in red. The red line shows the best LTE fit to the observed spectra (represented by the black lines). The data have been smoothed up to 3 km s^{-1} for an optimal line visualization. The blue lines show the spectra including the emission of all the molecules searched toward G+0.693. Note that these lines are tagged with their corresponding molecular compound in pink.

are totally clean (Figure 3, Appendix A) and above the 5σ level in integrated intensity. We derived a total column density of $(4 \pm 2) \times 10^{13}$ cm^{-2} (Table 2).

In the case of CH_3SH, the the fit was carried out separating the targeted lines into its $K_a = 0$ and $K_a = 1$ levels[14]. The brightest transitions fall into the 3 mm and 2 mm bands as presented in Figure 4 and Table 5 (Appendix B). Note that the agreement between the predicted and observed spectra is excellent for all clean transitions. The column density using the $K_a = 0$ and $K_a = 1$ levels is $(6.5 \pm 0.2) \times 10^{14}$ cm^{-2} (Table 2). This gives a ratio of CH_3SH/g-$C_2H_5SH = 16 \pm 7$. Note that the column density of $K_a = 2$ and remaining transitions in CH_3SH contribute less than a 10% in the total determined.

Finally, we note that both ^{13}C and ^{34}S isotopologues of CH_3SH have also been detected with a few clean lines and will be presented in a forthcoming paper (L. Colzi et al. 2021, in preparation).

3.3. Molecular Abundances and Comparison with Their O-bearing Analogs

To derive the fractional abundances of these species relative to H_2, we have assumed a H_2 column density of $N_{H_2} = 1.35 \times 10^{23}$ cm^{-2} (Martín et al. 2008). This gives $\sim 3 \times 10^{-10}$, $\sim 1 \times 10^{-10}$, and $\sim 5 \times 10^{-9}$ for g-C_2H_5SH, t-HC(O)SH, and CH_3SH, respectively (Table 2).

In Figure 2 we have plotted these values and compared them with the abundances obtained for their OH molecular analogs, namely, C_2H_5OH (ethanol), HC(O)OH (formic acid), and CH_3OH (methanol). We obtained a ratio $CH_3OH/CH_3SH = 23$, $C_2H_5OH/C_2H_5SH = 15$, and $HC(O)OH/HC(O)SH = 13$. Although these OH analogs are more abundant by a factor $\geqslant 10$, the resulting trend is strikingly similar. Note, however, that this trend is lost when we compare molecules such as carbon

[14] The moments of inertia of CH_3SH frame it in the limiting prolate case, $\kappa = (2B - A - C)/(A - C) \approx -0.988$.

Table 1
Lines of t-HC(O)SH Detected toward G+0.693 with Their Corresponding Quantum Numbers (QNs), Logarithm of the Einstein Coefficients (log A_{ul}) , Degeneracy (g_u), and Energy (E_u) of the Upper State

Rest Frequency (MHz)	QNs[a]	g_u	E_u (K)	log A_{ul} (s^{-1})	rms (mK)	$\int T_A^* d\nu$[b] (mK km s^{-1})	S/N[b]	Comments
34248.82	$3_{1,3} \rightarrow 2_{1,2}$	7	4.3	−6.4784	1.4	56	7.3	clean transition
35915.48	$3_{1,2} \rightarrow 2_{1,1}$	7	4.4	−6.4164	1.4	58	7.6	blended with $HOCH_2CH_2OH$
45659.99	$4_{1,4} \rightarrow 3_{1,3}$	7	6.0	−6.0647	2.4	88	13.4	clean transition
46737.73	$4_{0,4} \rightarrow 3_{0,3}$	7	3.4	−6.0064	2.6	122	8.6	clean transition
71800.18	$6_{1,5} \rightarrow 5_{1,4}$	13	11.3	−5.4428	3.5	121	6.3	clean transition
81630.08	$7_{0,7} \rightarrow 6_{0,6}$	15	11.8	−5.2587	3.4	153	8.2	slightly blended with CH_3CH_2CHO
83749.29	$7_{1,6} \rightarrow 6_{1,5}$	15	14.8	−5.2342	3.4	116	11.8	slightly blended with CH_3COOH
91251.84	$8_{1,8} \rightarrow 7_{1,7}$	17	18.1	−5.1166	1.7	104	11.2	slightly blended with $(CH_2OH)_2$ and unidentified species
93505.09	$8_{2,7} \rightarrow 7_{2,6}$	17	26.5	−5.1061	1.4	46	6.0	blended with $CH_3^{18}OH$

Notes. The integrated signal ($\int T_A^* d\nu$) and rms noise level are also provided and used to calculate the signal-to-noise ratio (S/N) of the detections.
[a] $J''_{K_a'' K_c''} \rightarrow J'_{K_a' K_c'}$ (where the double prime indicates the upper state).
[b] S/N is calculated from the integrated signal and noise level $\sigma = \text{rms}\sqrt{\delta v\ FWHM}$, where δv is the velocity resolution of the spectra.

Table 2
Physical Parameters of the Species Derived by LTE Analysis in MADCUBA

Molecular Formula	N ($\times 10^{13}$ cm^{-2})	T_{ex} (K)	v_{LSR} (km s^{-1})	FWHM (km s^{-1})	Abundance ($\frac{N(X)}{N(H_2)} \times 10^{-10}$)
trans − HC(O)SH	1.6 ± 0.1	10 ± 1	69.0 [a]	21.0 [a]	1.2 ± 0.2
cis − HC(O)SH	⩽0.3	10.0	69.0 [a]	21.0 [a]	⩽0.2
g − C_2H_5SH	4 ± 2	10 ± 5	69.0 [a]	20.0[a]	3 ± 1
a − C_2H_5SH	⩽2.3	9.91	69.0 [a]	20.0 [a]	⩽1.7
CH_3SH, $K_a = 0$	46.8 ± 0.5	8.5 ± 0.1	68.0 ± 0.1	21.2 ± 0.3	⋯
CH_3SH, $K_a = 1$	18.6 ± 0.7	14.9 ± 0.5	68.8 ± 0.3	22.0 ± 0.7	⋯
CH_3SH	65 ± 2	⋯	⋯	⋯	48 ± 5
t − HCOOH	20 ± 4	10 ± 2	68 ± 2	22 ± 5	15 ± 4

Note.
[a] Value fixed in the fit.

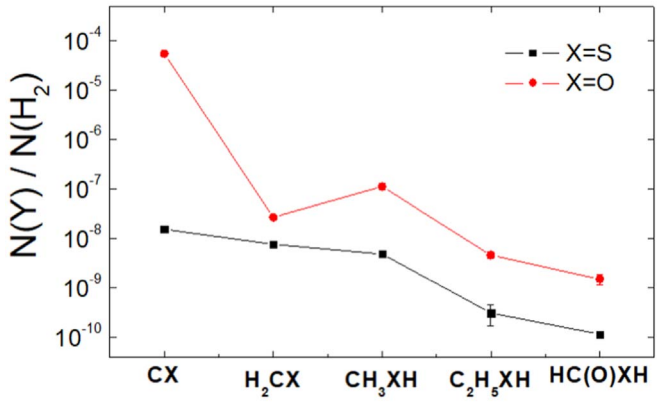

Figure 2. Molecular abundances with respect to H_2 for the reported detections and their OH analogs (CH_3OH, C_2H_5OH, and HC(O)OH) including CS, CO, H_2CO, and H_2CS. The lines that connect each dot do not have any physical meaning but are just a visual aid.

monosulfide (CS) and thioformaldehyde (H_2CS) with their O-bearing analogs, resulting in $H_2CO/H_2CS = 3.5$ and $CO/CS = 3.5 \times 10^3$ (Figure 2).

Since CH_3OH, C_2H_5OH, H_2CO, CO, and CS are optically thick toward G+0.693, the column density of these molecules was inferred from $CH_3^{18}OH$, $^{13}CH_3CH_2OH$, $H_2C^{18}O$, $C^{18}O$, and $^{13}C^{34}S$. It was assumed $^{16}O/^{18}O = 250$ and $^{12}C/^{13}C = 21$ (Armijos-Abendaño et al. 2015) and $^{32}S/^{34}S = 22$ (Wilson 1999). For HC(O)OH, the main isotopologue of HC(O)OH was employed as the ratio $H^{12}C(O)OH/H^{13}C(O)OH$, which is consistent with the $^{12}C/^{13}C$ ratio. For the sulfur analogs, except CS, we do not expect opacity issues due to their much lower abundances. The fit and transitions selected for these molecules are listed in Appendix B (Figures 5 and 6 and Tables 6, 7, 8, 9, and 10).

4. Discussion

4.1. Comparison with Previous Observations

We have compared different column density ratios obtained between the S-bearing compounds measured toward G+0.693 and two other sources, namely, Orion KL (Kolesniková et al. 2014) and Sgr B2(N2) (Müller et al. 2016; see Table 3).

From this table, we find that all abundance ratios measured in G +0.693 are strikingly similar. For instance, when we compare SH-bearing molecules with their OH analogs (CH_3OH/CH_3SH and C_2H_5OH/C_2H_5SH) we recover the trend already found in Figure 2, which might indicate a similar chemistry between OH- and SH-bearing species. The CH_3OH/CH_3SH ratio measured in G+0.693 is a factor of 5 lower than those found in Sgr B2(N2) and Orion KL, which indicates that G+0.693 is richer in sulfur-bearing species than the two massive hot cores. This may be related to the fact that the chemistry of this cloud is affected by large-scale shocks (Requena-Torres et al. 2006; Zeng et al. 2018).

Table 3
Relative Abundances of Molecules and Comparison with Other Sources

Source	CH_3SH/C_2H_5SH	CH_3OH/C_2H_5OH	CH_3OH/CH_3SH	C_2H_5OH/C_2H_5SH
G+0.693	16 ± 7	24 ± 4[c,d]	23 ± 3[c]	15 ± 7[d]
Sgr B2(N2)[a]	$\geqslant 21$	20	118	$\geqslant 125$
Orion KL[b]	5	31	120	20

Notes.
[a] Data taken from Müller et al. (2016).
[b] Data taken from Kolesniková et al. (2014).
[c] Data inferred from $CH_3^{18}OH$ assuming $^{16}O/^{18}O = 250$ (Armijos-Abendaño et al. 2015).
[d] Data inferred from $^{13}CH_3CH_2OH$ assuming $^{12}C/^{13}C = 21$ (Armijos-Abendaño et al. 2015).

Since sulfur is heavily depleted on grains (possibly in the form of S_8 and other sulfur allotropes; Shingledecker et al. 2020), the sputtering of dust grains induced by shocks could liberate a significant fraction of the locked sulfur.

The C_2H_5OH/C_2H_5SH ratio is comparable to the value determined toward Orion KL while there is a difference by a factor of 10 between G+0.693 and the upper limit toward Sgr B2(N2). All these ratios suggest that sulfur is less incorporated into molecules than oxygen, which again might be due to the fact that a significant fraction of sulfur is locked up in grains.

4.2. Interstellar Chemistry of Thiols

In order to understand the chemistry of S-bearing compounds, different models have been proposed based on the simple molecules detected in the gas phase (Müller et al. 2016; Gorai et al. 2017; Lamberts 2018; Laas & Caselli 2019). CH_3SH is thought to be formed on grain surfaces by sequential hydrogenations starting from CS:

$$CS + H \rightarrow HCS$$
$$HCS + H \rightarrow H_2CS$$
$$H_2CS + H \rightarrow CH_3S$$
$$CH_3S + H \rightarrow CH_3SH.$$

The last step could also yield other products, but theoretical calculations show a branching ratio (br) of ~75% for CH_3SH (Lamberts 2018). This is a viable mechanism since approximately half of the CS present in the ices is available to undergo hydrogenation, while the other half is converted to OCS (Palumbo et al. 1997). Once formed, CH_3SH could remain stored in the ices until released by grain sputtering in the large-scale shocks present in G+0.693 (Requena-Torres et al. 2006; Zeng et al. 2020).

Likewise, ethyl mercaptan is proposed to be formed by radical–radical reactions (Müller et al. 2016; Gorai et al. 2017) such as

$$C_2H_5 + SH \rightarrow C_2H_5SH$$
$$CH_3 + CH_2SH \rightarrow C_2H_5SH.$$

Observations of the reactants could give us a hint of the dominant reaction based on the measured column densities. However, chemical modeling is needed to understand the efficiency of these formation routes. Note that CH_2SH is the main product of the hydrogenation of H_2CS (Lamberts 2018).

To our knowledge, there is no information available in the literature about the chemistry of HC(O)SH. However, we can make a guess and assume similar astrochemical pathways for the SH-based species as the ones for their OH analogs. A possible pathway to HC(O)SH could mimic the formation of HC(O)OH. Ioppolo et al. (2011) showed that the formation of HC(O)OH starts from CO and the OH radical in the ice. The thiol-equivalent reaction would be

$$CO + SH \rightarrow HSCO \xrightarrow{H} HC(O)SH.$$

The first step has been found to be efficient by Adriaens et al. (2010), but further experimental and/or theoretical work is needed to investigate whether HSCO could be hydrogenated further.

Another possibility could be

$$HCO + SH \rightarrow HCOSH$$

or

$$OCS \xrightarrow{2H} HC(O)SH.$$

The first reaction was initially proposed for HC(O)OH by Garrod & Herbst (2006) and could be a viable mechanism since SH can be formed on surfaces from S+H or H+H_2S via tunneling (Vidal et al. 2017). The second involves the sequential hydrogenation of OCS, which is a molecule detected in ices (Palumbo et al. 1997) and it is moderately abundant in the gas phase in G+0.693 ($N > 10^{15}$ cm^{-2}; Armijos-Abendaño et al. 2015). Theoretical studies about these chemical networks are currently under work and will be presented in a forthcoming paper (G. Molpeceres et al. 2021, in preparation).

4.3. Implications for Theories on the Origin of Life

As it was previously stated, thioacids and thioesters have been proposed as key agents in the polymerization of amino acids into peptides and proteins (Foden et al. 2020; Muchowska & Moran 2020). In some of these works, it is stressed the importance of cystein, $HSCH_2CH(NH_2)COOH$, as the primary organic source of sulfide in biology and a key catalyst in the abiotic polymerization of peptides. Smaller thiols such as CH_3SH and C_2H_5SH are also believed to play a key role in prebiotic chemistry and in theories about the origin of life, since they are precursors for the synthesis of the amino acids methionine and ethionine (Parker et al. 2011). In turn, HC(O)SH could be an important ingredient in the phosphorylation of nucleosides as demonstrated by Lohrmann & Orgel (1968).

The idea of an extraterrestrial delivery of SH compounds onto Earth, is supported by the detection of CH_3SH in Murchinson carbonaceous chondrite (Tingle et al. 1991) and in the coma of the 67P/Churyumov–Gerasimenko comet (Calmonte et al. 2016). In the latter, C_2H_6S was also detected (either in the form of C_2H_5SH or CH_3SCH_3, dimethyl sulfide) with an abundance ratio $CH_3SH/C_2H_6S \sim 10$ that is consistent with the value obtained in G+0.693 (Table 3). This resemblance could be possibly indicate a presolar origin of these compounds. Still, further studies are required within other regions in the ISM and planetary bodies to make a proper connection.

In summary, not only have our observations confirmed the presence of sulfur-bearing complex organics such as CH_3SH and C_2H_5SH, but they also have revealed the existence of the simplest thioacid known, HC(O)SH, in the ISM.

We acknowledge the anonymous reviewers for their useful comments that have helped to improved our manuscript. L.F.R.-A. acknowledges support from a JAE-intro ICU studentship funded by the Spanish National Research Council (CSIC). L.F.R.-A., V.M.R., and L.C. also acknowledge support from the Comunidad de Madrid through the Atracción de Talento Investigador Modalidad 1 (Doctores con experiencia) Grant (COOL: Cosmic Origins Of Life; 2019-T1/TIC-15379; PI: V.M.Rivilla). I.J.-S. and J.M.-P. have received partial support from the State Research Agency (AEI) through project numbers PID2019-105552RB-C41 and MDM-2017-0737 Unidad de Excelencia "María de Maeztu"—Centro de Astrobiología (CSIC-INTA). P.d.V. and B.T. thank the support from the European Research Council through Synergy Grant ERC-2013-SyG, G.A. 610256 (NANOCOSMOS) and from the Spanish Ministerio de Ciencia e Innovación (MICIU) through project PID2019-107115GB-C21. B.T. also thanks the Spanish MICIU for funding support from grants AYA2016-75066-C2-1-P and PID2019-106235GB-I00.

Facilities: IRAM 30 m, Yebes 40 m.

Software: MADCUBA.

Appendix A
Detections of C_2H_5SH and CH_3SH in G+0.693

In Figures 3 and 4 and Tables 4 and 5 the fit of g-C_2H_5SH and CH_3SH is shown. The fitting procedure followed has been the same as t-HC(O)SH, explained in the main text.

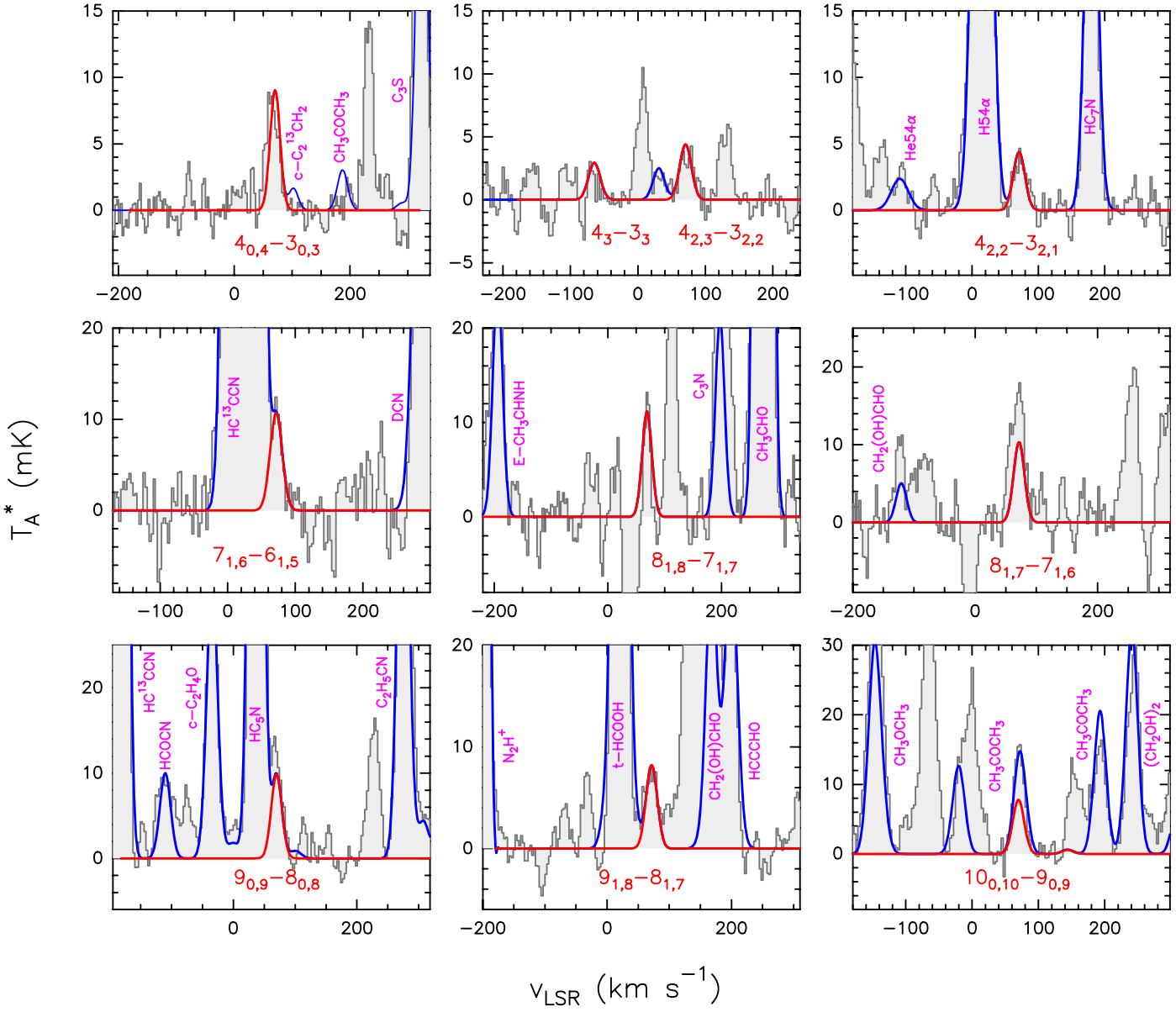

Figure 3. Cleanest and brightest lines of g-C_2H_5SH detected toward G+0.693. The red line shows the best LTE fit to the observed spectra (represented by the black lines) with their corresponding quantum numbers in red (J_{K_a,K_c}; see Table 4 for a description of their tunneling states). The data have been smoothed up to 3 km s^{-1} for an optimal line visualization. The blue lines show the spectra including the emission of all the molecules searched toward the cloud. Note that these lines are tagged with their corresponding molecular compound in pink.

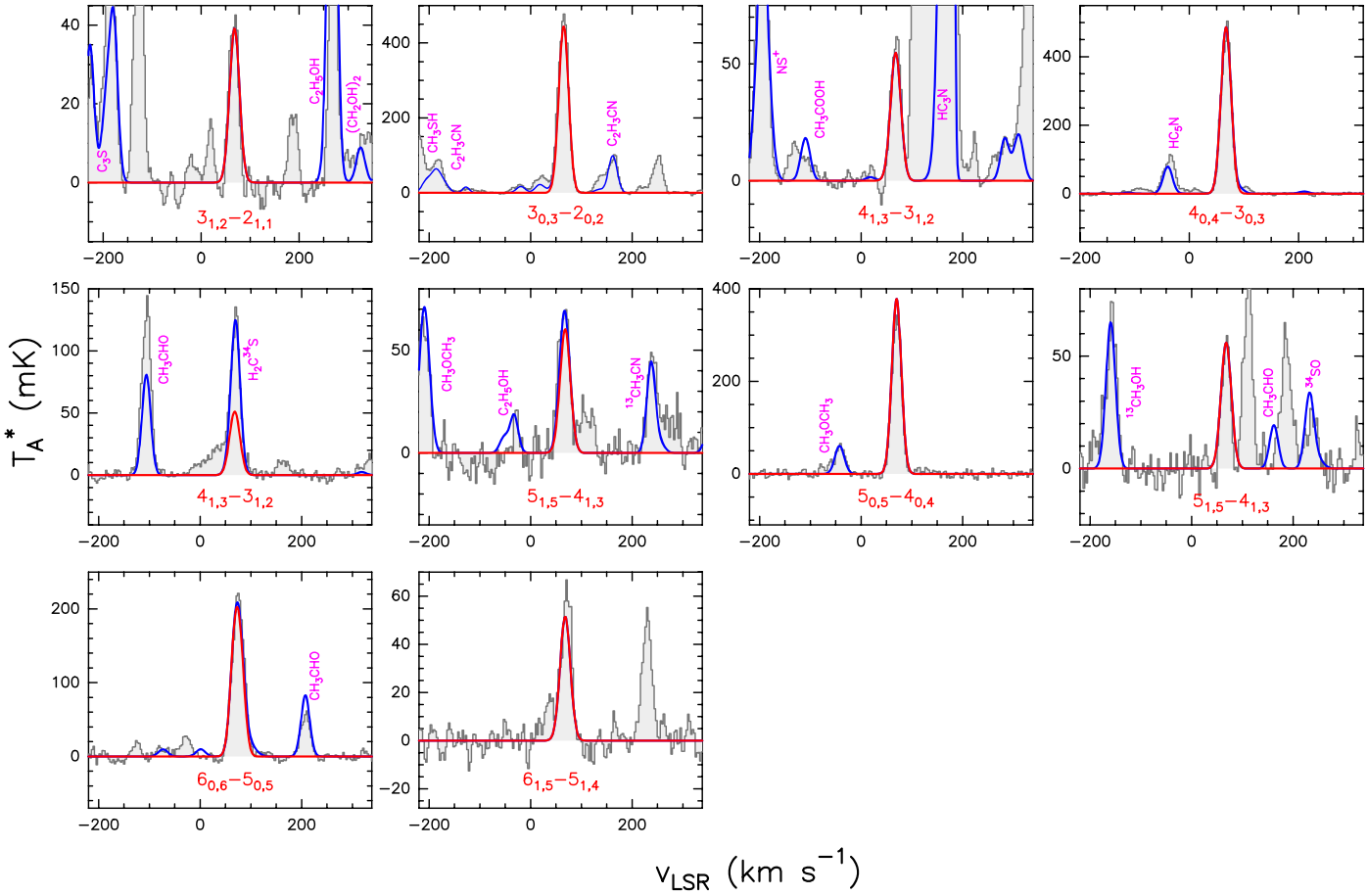

Figure 4. Cleanest and brightest lines of CH_3SH detected toward G+0.693. The red line shows the best LTE fit to the observed spectra (represented by the black lines) with their corresponding quantum numbers in red (J_{K_a,K_c}; see Table 5 for the description of their torsional states). The data have been smoothed up to 3 km s^{-1} for an optimal line visualization. The blue lines show the spectra including the emission of all the molecules searched toward the cloud. Note that these lines are tagged with their corresponding molecular compound in pink.

Table 4
Lines of g-C_2H_5SH Detected toward G+0.693 with Their Corresponding QNs and Tunneling States (TSs), log A_{ul}, g_u, and E_u

Rest Frequency (MHz)	QNs	TS $\nu'' \rightarrow \nu'$	g_u	E_u (K)	log A_{ul} (s^{-1})	rms (mK)	$\int T_A^* d\nu$ (mK km s^{-1})	S/N	Comments
40499.173	$4_{0,4} \rightarrow 3_{0,3}$	$1 \rightarrow 1$	9	3.0	−6.1161	1.4	225	29	clean transition[a]
40499.591	$4_{0,4} \rightarrow 3_{0,3}$	$0 \rightarrow 0$	9	2.9	−6.1163	1.4	…	…	…
40558.849	$4_{2,3} \rightarrow 3_{2,2}$	$1 \rightarrow 1$	9	7.6	−6.2391	1.2	107	16	clean transition[a]
40559.284	$4_{2,3} \rightarrow 3_{2,2}$	$0 \rightarrow 0$	9	7.5	−6.2392	1.2	…	…	…
40576.963	$4_{3,2} \rightarrow 3_{3,1}$	$1 \rightarrow 1$	9	13.2	−6.2004	1.2	72	11	clean transition[a]
40577.299	$4_{3,1} \rightarrow 3_{3,0}$	$1 \rightarrow 1$	9	13.2	−6.2004	1.2	…	…	…
40577.432	$4_{3,2} \rightarrow 3_{3,1}$	$0 \rightarrow 0$	9	13.2	−6.2004	1.2	…	…	…
40577.769	$4_{3,1} \rightarrow 3_{3,0}$	$0 \rightarrow 0$	9	13.2	−6.2004	1.2	…	…	…
40622.316	$4_{2,2} \rightarrow 3_{2,1}$	$1 \rightarrow 1$	9	7.6	−6.2370	1.2	107	16	clean transition[a]
40622.792	$4_{2,2} \rightarrow 3_{2,1}$	$0 \rightarrow 0$	9	7.5	−6.2371	1.2	…	…	…
72466.861	$7_{1,6} \rightarrow 6_{1,5}$	$1 \rightarrow 1$	15	11.7	−5.3458	2.8	261	17	clean transition[a]
72468.152	$7_{1,6} \rightarrow 6_{1,5}$	$0 \rightarrow 0$	15	11.6	−5.3459	2.8	…	…	…
79204.501	$8_{1,8} \rightarrow 7_{1,7}$	$1 \rightarrow 1$	17	14.6	−5.2243	1.8	204	24	clean transition[a]
79204.501	$8_{1,8} \rightarrow 7_{1,7}$	$0 \rightarrow 0$	17	14.6	−5.2243	1.8	…	…	…
82782.441	$8_{1,7} \rightarrow 7_{1,6}$	$1 \rightarrow 1$	17	15.2	−5.1667	1.8	233	30	slightly blended with unidentified line[a]
82783.912	$8_{1,7} \rightarrow 7_{1,6}$	$0 \rightarrow 0$	17	15.1	−5.1668	1.4	…	…	…
90516.341	$9_{0,9} \rightarrow 8_{0,8}$	$1 \rightarrow 1$	19	17.6	−5.0412	1.2	223	34	slightly blended with unidentified line[a]
90516.926	$9_{0,9} \rightarrow 8_{0,8}$	$0 \rightarrow 0$	19	17.5	−5.0414	1.2	…	…	…
93082.083	$9_{1,8} \rightarrow 8_{1,7}$	$1 \rightarrow 1$	19	19.1	−5.0096	2.0	191	18	clean transition[a]
93083.720	$9_{1,8} \rightarrow 8_{1,7}$	$0 \rightarrow 0$	19	19.1	−5.0097	2.0	…	…	…

Table 4
(Continued)

Rest Frequency (MHz)	QNs	TS $\nu'' \rightarrow \nu'$	g_u	E_u (K)	log A_{ul} (s^{-1})	rms (mK)	$\int T_A^* d\nu$ (mK km s^{-1})	S/N	Comments
100391.240	$10_{0,10} \rightarrow 9_{0,9}$	$1 \rightarrow 1$	21	21.9	−4.9042	1.8	171	17	blended with CH_3COCH_3[a]
100391.791	$10_{0,10} \rightarrow 9_{0,9}$	$0 \rightarrow 0$	21	21.8	−4.9042	1.8	⋯	⋯	⋯

Notes. $\int T_A^* d\nu$ and rms are also provided and used to calculate the S/N of the detected lines.
[a] In these cases, the lines are composed by a blend of individual g-C_2H_5SH lines. Here, S/N is calculated according to Figure 3.

Table 5
Lines of CH_3SH Detected toward G+0.693 with Their Corresponding Quantum Numbers (QNs) and Torsional Symmetry (T_s), Logarithm of the Einstein Coefficients (log A_{ul}), Degeneracy (g_u), and Energy (E_u) of the Upper State

Rest Frequency (MHz)	QNs	T_s	g_u	E_u (K)	log A_{ul} (s^{-1})	rms (mK)	I_{peak} (mK)	S/N	Comments
75085.898	$3_{1,2} \rightarrow 2_{1,1}$	A^+	7	8.7	−5.5086	2.7	39	14	clean transition
75862.889	$3_{0,3} \rightarrow 2_{0,2}$	A^+	7	3.6	−5.4444	2.3	260	113	clean transition
75864.422	$3_{0,3} \rightarrow 2_{0,2}$	E	7	5.1	−5.4443	2.3	221	96	clean transition
100110.219	$4_{1,3} \rightarrow 3_{1,2}$	A^+	9	12.3	−5.0966	3.1	55	18	clean transition
101139.150	$4_{0,4} \rightarrow 3_{0,3}$	A^+	9	7.3	−5.0554	2.9	271	93	clean transition
101139.655	$4_{0,4} \rightarrow 3_{0,3}$	E	9	8.7	−5.0543	2.9	230	79	clean transition
101284.366	$4_{1,3} \rightarrow 3_{1,2}$	E	9	13.5	−5.0818	2.9	51	18	blended with $H_2C^{34}S$
125130.863	$5_{1,5} \rightarrow 4_{1,3}$	A^+	11	17.1	−4.7869	6.2	61	10	slightly blended with HC_5N
126403.834	$5_{0,5} \rightarrow 4_{0,4}$	E	11	13.6	−4.7556	6.4	183	29	clean transition
126405.676	$5_{0,5} \rightarrow 4_{0,4}$	A^+	11	12.2	−4.7556	6.4	215	34	clean transition
126683.419	$5_{1,5} \rightarrow 4_{1,9}$	A^+	11	18.4	−4.7707	6.5	56	9	clean transition
151654.218	$6_{0,6} \rightarrow 5_{0,5}$	E	13	19.6	−4.5123	5.4	116	22	clean transition
151660.047	$6_{0,6} \rightarrow 5_{0,5}$	A^+	13	18.2	−4.5123	5.4	136	25	clean transition
152129.018	$6_{1,5} \rightarrow 5_{1,4}$	E	13	24.4	−4.5210	4.5	52	12	clean transition

Note. The peak intensity (I_{peak}) and rms noise level are also provided and used to calculate the signal-to-noise ratio (S/N) of the detected lines.

Appendix B
Figures and Tables of $^{13}C^{34}S$, H_2CS, $H_2C^{18}O$, $CH_3^{18}OH$, and $^{13}CH_3CH_2OH$

We show a few of the intense lines selected within the targeted frequency coverage in G+0.693 for some of the species used in the molecular abundances calculations in Figure 2. Note that other visible lines not shown in these figures or tables are either heavily blended or in a bad part of the spectra.

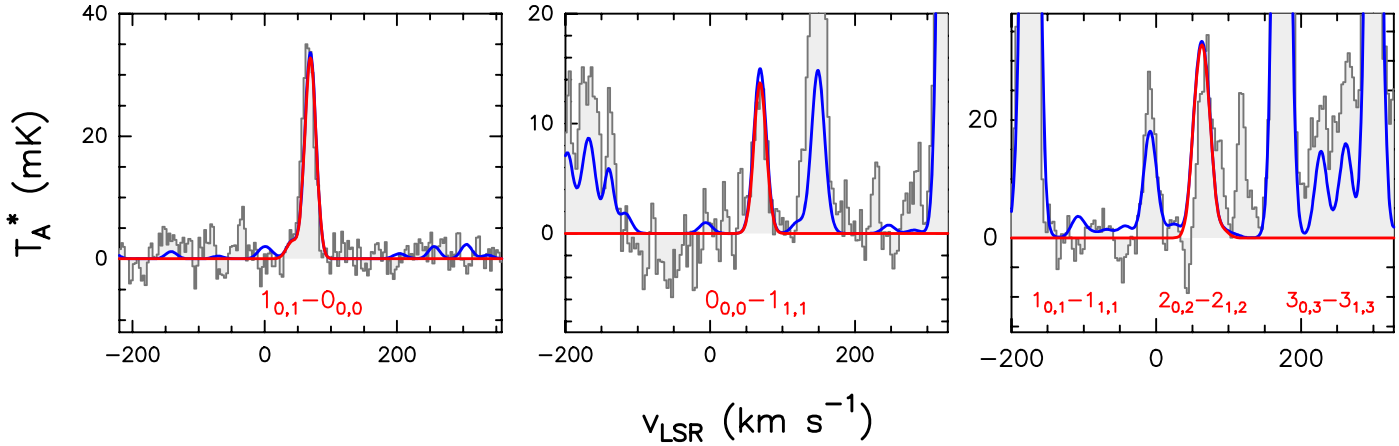

Figure 5. Selected lines of $CH_3^{18}OH$ detected toward G+0.693. Black, red, and blue lines represent the observational data, the individual lines of $CH_3^{18}OH$, and the global fit considering all the species detected, respectively. See Table 9 for a complete description of their quantum numbers).

Table 6
Lines of $^{13}C^{34}S$ Detected toward G+0.693 with Their Corresponding Spectroscopic Information and Parameters Derived from the LTE Fit

Rest Frequency (MHz)	QNs	g_u	E_u (K)	log A_{ul} (s^{-1})	rms (mK)	$\int T_A^* d\nu$ (mK km s^{-1})	S/N	Comments
45463.424	$1 \rightarrow 0$	3	0.0	−5.8546	2.0	364	>20	clean transition
90926.026	$2 \rightarrow 1$	5	2.0	−4.8723	2.5	854	>20	clean transition
136387.028	$3 \rightarrow 2$	7	6.6	−4.3141	2.1	796	>20	clean transition

Table 7
Lines of H_2CS Detected toward G+0.693 with $I_{peak} > 0.8$K and Their Corresponding Spectroscopic Information and Parameters Derived from the LTE Fit

Rest Frequency (MHz)	QNs	g_u	E_u (K)	log A_{ul} (s^{-1})	rms (mK)	I_{peak} (K)	S/N	Comments
101477.8048	$3_{1,3} \rightarrow 2_{1,2}$	21	2.0	−4.8996	2.9	1.213	>20	clean transition
103040.447	$3_{0,3} \rightarrow 2_{0,2}$	7	5.0	−4.8285	2.6	0.951	>20	clean transition
104617.027	$3_{1,2} \rightarrow 2_{1,1}$	27	18.2	−4.8599	2.1	1.169	>20	clean transition
135298.26	$4_{1,4} \rightarrow 3_{1,3}$	27	22.9	−4.4859	7.0	1.213	>20	clean transition
137371.21	$4_{0,4} \rightarrow 3_{0,3}$	9	9.9	−4.438	3.1	0.823	>20	clean transition
139483.68	$4_{1,3} \rightarrow 3_{1,2}$	27	23.2	−4.4462	2.7	1.197	>20	clean transition

Table 8
Lines of $H_2C^{18}O$ Detected toward G+0.693 with Their Corresponding Spectroscopic Information and Parameters Derived from the LTE Fit

Rest Frequency (MHz)	QNs	g_u	E_u (K)	log A_{ul} (s^{-1})	rms (mK)	$\int T_A^* d\nu$ (mK km s^{-1})	S/N	Comments
134435.920	$2_{1,2} \rightarrow 1_{1,1}$	15	2.0	−4.3361	6.7	839	>20	slightly blended with CH_3CHO
138770.86	$2_{0,2} \rightarrow 1_{0,1}$	5	3.3	−4.1697	2.7	814	>20	clean transition
143213.07	$2_{1,1} \rightarrow 1_{1,0}$	15	15.3	−4.2536	2.1	824	>20	clean transition

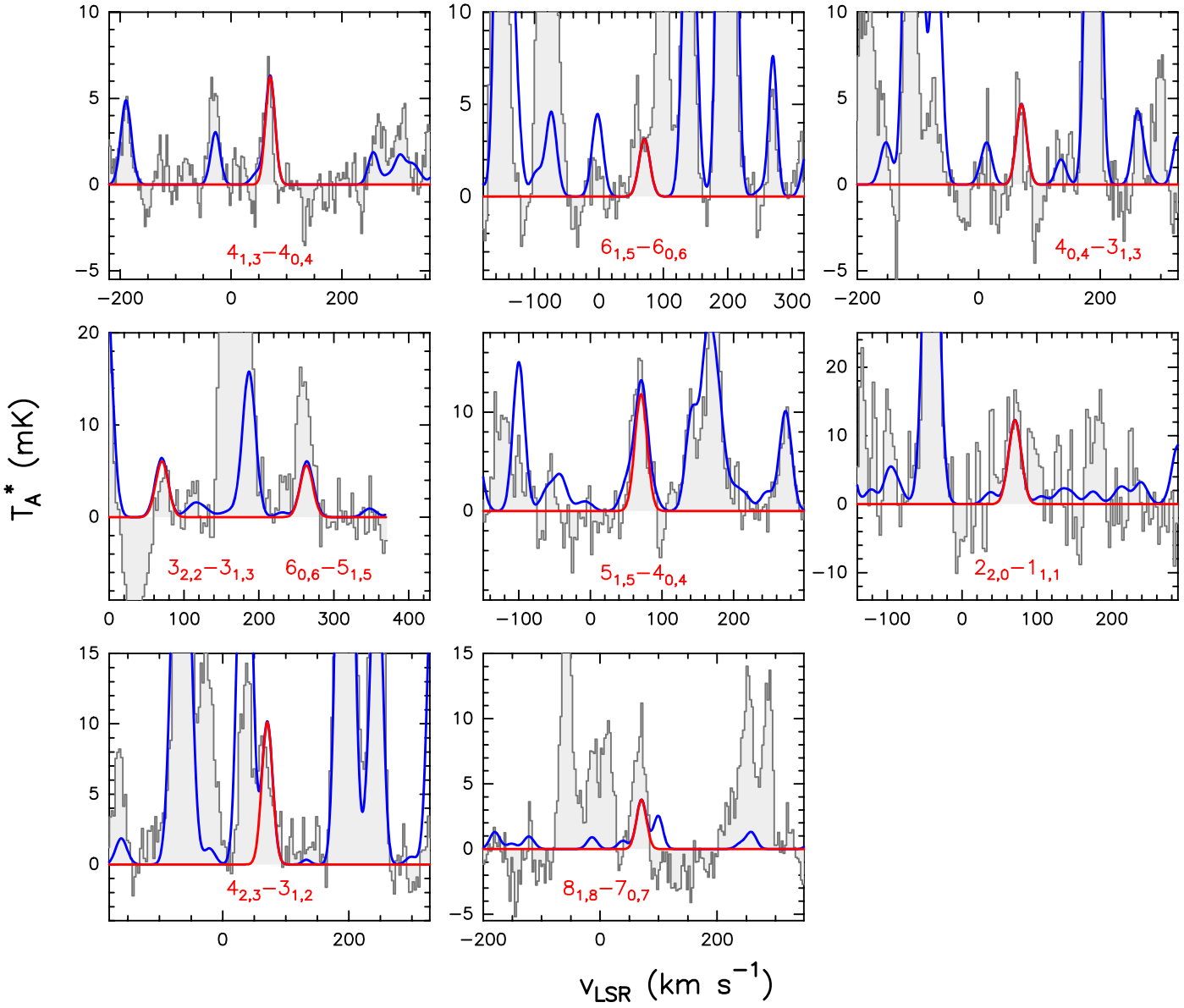

Figure 6. Selected lines of anti-$^{13}CH_3CH_2OH$ detected toward G+0.693. Black, red, and blue lines represent the observational data, the individual lines of $^{13}CH_3CH_2OH$, and the global fit with all species, respectively.

Table 9
Lines of $CH_3^{18}OH$ Detected toward G+0.693 with Their Corresponding Spectroscopic Information and Parameters Derived from the LTE Fit

Rest Frequency (MHz)	QNs	T_s	g_u	E_u (K)	log A_{ul} (s^{-1})	rms (mK)	$\int T_A^* d\nu$ (mK km s^{-1})	S/N	Comments
46364.313	$1_{0,1} \rightarrow 0_{0,0}$	A	12	0.0	−4.8985	2.8	709	>20	clean transition
93505.902	$2_{1,1} \rightarrow 1_{1,0}$	A	20	16.6	−5.6353	1.9	68	7	blended with t-HC(O)SH
150698.06	$1_{0,1} \rightarrow 1_{1,1}$	E	12	7.8	−4.7223	3.1	466	>20	clean transition
150704.121	$3_{0,3} \rightarrow 3_{1,3}$	E	28	19.0	−4.7330	3.1	127	8	clean transition
150704.173	$2_{0,2} \rightarrow 2_{1,2}$	E	20	12.3	−4.7266	3.1	328	19	clean transition

Table 10
Lines of anti-$^{13}CH_3CH_2OH$ Detected toward G+0.693 with Their Corresponding Spectroscopic Information and Parameters Derived from the LTE Fit

Rest Frequency (MHz)	QNs	g_u	E_u (K)	log A_{ul} (s^{-1})	rms (mK)	$\int T_A^* d\nu$ (mK km s^{-1})	S/N	Comments
32509.32	$4_{1,3} \rightarrow 4_{0,4}$	9	8.2	−6.4293	1.3	134	19	clean transition
40435.51	$6_{1,5} \rightarrow 6_{0,6}$	13	17.0	−6.2050	1.5	67	8	slightly blended with unidentified transition
44748.194	$4_{0,4} \rightarrow 3_{1,3}$	9	6.0	−6.3778	2.1	100	9	clean transition
82170.297	$6_{0,6} \rightarrow 5_{1,5}$	13	13.1	−5.4772	3.5	121	6	blended with unidentified transition
82223.219	$3_{2,2} \rightarrow 3_{1,3}$	7	6.0	−5.5620	2.8	130	9	clean transition
102934.258	$5_{1,5} \rightarrow 4_{0,4}$	11	8.2	−5.1178	2.6	253	18	clean transition
113369.368	$2_{2,0} \rightarrow 1_{1,1}$	5	2.1	−4.9878	6.8	262	7	clean transition
143297.176	$4_{2,3} \rightarrow 3_{1,2}$	9	6.3	−4.8286	2.2	216	18	clean transition
144465.114	$8_{1,8} \rightarrow 7_{0,7}$	17	22.7	−4.6339	1.7	81	9	blended with unidentified transition

ORCID iDs

Lucas F. Rodríguez-Almeida https://orcid.org/0000-0002-9785-703X
Izaskun Jiménez-Serra https://orcid.org/0000-0003-4493-8714
Víctor M. Rivilla https://orcid.org/0000-0002-2887-5859
Jesús Martín-Pintado https://orcid.org/0000-0003-4561-3508
Belén Tercero https://orcid.org/0000-0002-4782-5259
Sergio Martín https://orcid.org/0000-0001-9281-2919

References

Adriaens, D. A., Goumans, T. P. M., Catlow, C. R. A, et al. 2010, J. Phys. Chem. C, 114, 1892
Armijos-Abendaño, J., Martín-Pintado, J., Requena-Torres, M. A., et al. 2015, MNRAS, 446, 3842
Asplund, M., Grevesse, N., Sauval, A., et al. 2009, ARA&A, 47, 481
Calmonte, U., Altwegg, K., Balsiger, H., et al. 2016, MNRAS, 462, S253
Chandru, K., Gilbert, A., Butch, C., et al. 2016, Sci. Rep., 6, 29883
Endres, C. P., Schlemmer, S., Schilke, P., et al. 2016, JMoSp, 327, 95
Foden, C. S., Islam, S., Fernández-García, C., et al. 2020, Sci, 370, 865
Garrod, R. T., & Herbst, E. 2006, A&A, 457, 927
Gibb, E., Nummelin, A., Irvine, W. M., et al. 2000, ApJ, 545, 309
Gorai, P., Das, A., Sivaraman, B., et al. 2017, ApJ, 836, 70
Herbst, E., & Van Dishoeck, E. F. 2009, ARA&A, 47, 427
Hocking, W. H., & Winnewisser, G. 1976, ZNatA, 31a, 995
Ioppolo, S., Van Boheemen, Y., Cuppen, H., et al. 2011, MNRAS, 413, 2281
Jabri, A., Tercero, B., Margulès, L., et al. 2020, A&A, 644, A102
Jiménez-Escobar, A., Muñoz Caro, G. M., & Chen, Y. J. 2014, MNRAS, 443, 343
Jiménez-Serra, I., Martín-Pintado, J., Rivilla, V. M., et al. 2020, AsBio, 20, 1048
Kolesniková, L., Tercero, B., Cernicharo, J., et al. 2014, ApJL, 784, L7
Laas, J. C., & Caselli, P. 2019, A&A, 624, A108
Lamberts, T. 2018, A&A, 615, L2
Leman, L. J., & Ghadiri, M. R. 2017, Synlett, 28, 68
Linke, R., Frerking, M. A., & Thaddeus, P. 1979, ApJL, 234, L139
Lohrmann, R., & Orgel, L. E. 1968, Sci, 161, 64
Majumdar, L., Gratier, P., Vidal, T., et al. 2016, MNRAS, 458, 1859
Margulès, L., Ilyushin, V. V., McGuire, B. A., et al. 2020, JMoSp, 371, 111304
Martín, S., Martín-Pintado, J., Blanco-Sánchez, C., et al. 2019, A&A, 631, A159
Martín, S., Requena-Torres, M. A., Martín-Pintado, J., et al. 2008, ApJ, 678, 245
Motiyenko, R., Belloche, A., Garrod, R., et al. 2020, A&A, 642, A29
Muchowska, K. B., & Moran, J. 2020, Sci, 370, 767
Müller, H. S. P., Belloche, A., Li-Hong, X., et al. 2016, A&A, 587, A92
Palumbo, M. E., Geballe, T. R., & Tielens, A. G. G. M. 1997, ApJ, 479, 839
Parker, E. T., Cleaves, H. J., Callahan, M. P., et al. 2011, OLEB, 41, 201
Requena-Torres, M. A., Martín-Pintado, J., Martín, S., et al. 2008, ApJ, 672, 352
Requena-Torres, M. A., Martín-Pintado, J., Rodríguez-Fernández, N. J., et al. 2006, A&A, 455, 971
Rivilla, V. M., Jiménez-Serra, I., Zeng, S., et al. 2018, MNRAS, 475, L30
Rivilla, V. M., Martín-Pintado, J., Jiménez-Serra, I., et al. 2019, MNRAS, 483, L114
Rivilla, V. M., Martín-Pintado, J., Jiménez-Serra, I., et al. 2020, ApJL, 899, L28
Shalayel, I., Youssef-Saliba, S., Vazart, F., et al. 2020, Eur.J. Org. Chem., 20, 3019
Shingledecker, C. N., Lamberts, T., Laas, J. C., et al. 2020, ApJ, 888, 52
Sinclair, M. W., Fourikis, N., Ribes, J. C., et al. 1973, AuJPh, 26, 85
Tercero, F., López-Pérez, J. A., Gallego, J. D., et al. 2021, A&A, 645, A37
Tingle, N., Becker, C. H., & Ripudaman, M. 1991, Metic, 26, 117
Vidal, T. H. G., Loison, J.-C., Jaziri., A. Y., et al. 2017, MNRAS, 469, 435
Wilson, T. L. 1999, RPPh, 62, 143
Xu, L. H., Lees, R. M., Grabbe, G. T., et al. 2012, JChPh, 137, 104313
Zakharenko, O., Ilyushin, V. V., Lewen, F., et al. 2019, A&A, 629, A73
Zeng, S., Jiménez-Serra, I., Rivilla, V. M., et al. 2018, MNRAS, 478, 2962
Zeng, S., Zhang, Q., Jiménez-Serra, I., et al. 2020, MNRAS, 497, 4896